nanomaterials

MDPI

Article

Highly Sensitive Acetone Gas Sensors Based on Erbium-Doped Bismuth Ferrite Nanoparticles

Xiaolian Liu *, Jing Li, Lanlan Guo and Guodong Wang *

School of Physics and Electronic Information Engineering, Henan Polytechnic University, Jiaozuo 454003, China
* Correspondence: liuxl123@hpu.edu.cn (X.L.); wgd@hpu.edu.cn (G.W.); Tel.: +86-13290706609 (X.L.)

Abstract: The acetone-sensing performance of $BiFeO_3$ is related to structural phase transformation, morphology and band gap energy which can be modulated by rare-earth ions doping. In this work, $Bi_{1-x}Er_xFeO_3$ nanoparticles with different amounts of Er doping were synthesized via the sol-gel method. The mechanism of Er doping on acetone-sensing performance of $Bi_{1-x}Er_xFeO_3$ (x = 0, 0.05, 0.1 and 0.2) sensors was the focus of the research. The optimal working temperature of $Bi_{0.9}Er_{0.1}FeO_3$ (300 °C) was decreased by 60 °C compared to $BiFeO_3$ (360 °C). The $Bi_{0.9}Er_{0.1}FeO_3$ sample demonstrated the optimal response to 100 ppm acetone (43.2), which was 4.8 times that of pure BFO at 300 °C. The primary reason, which enhances the acetone-sensing performance, could be the phase transformation induced by Er doping. The lattice distortions induced by phase transformation are favorable to increasing the carrier concentration and mobility, which will bring more changes to the hole-accumulation layer. Thus, the acetone-sensing performance of $Bi_{0.9}Er_{0.1}FeO_3$ was improved.

Keywords: bismuth ferrite nanoparticles; Er doping; acetone gas sensor; morphotropic phase boundary

Citation: Liu, X.; Li, J.; Guo, L.; Wang, G. Highly Sensitive Acetone Gas Sensors Based on Erbium-Doped Bismuth Ferrite Nanoparticles. *Nanomaterials* **2022**, *12*, 3679. https://doi.org/10.3390/nano12203679

Academic Editor: Sergei Kulinich

Received: 31 August 2022
Accepted: 17 October 2022
Published: 20 October 2022

1. Introduction

Acetone is a common volatile organic compound that is widely used in the chemical industry and laboratories. However, long-term exposure to acetone or excessive inhalation of acetone causes great damage to the skin, nervous system, and breathing system, which leads to dermatitis, headache, nausea and coma [1]. Thus, the detection of acetone is highly significant for human health. Meanwhile, the detection of acetone can be used in the diagnosis of some diseases. For example, in the breath of diabetes patients, the concentration of acetone is more than twice as much as that of healthy people [2]. Compared to blood tests, acetone gas sensing is quick, easy, and noninvasive. Consequently, great attention has been paid to the study of acetone gas sensors. Plenty of oxides have been reported to show acetone-sensing performance, such as ZnO, SnO_2, Co_3O_4, Fe_2O_3, WO_3 and so on. Some strategies have been adopted to optimize gas sensing performance, such as designing nanomaterial with special morphology and structure [3,4], preparation of composite materials [5], doping with rare-earth and noble-metal ions [6,7] and decorating with other nanomaterial [8]. However, studies have shown that binary metal oxides display excellent gas sensing performance, but suffer from high operating temperature and relatively poor stability [9,10]. Consequently, the study of the acetone gas sensor based on ternary oxides has been of great interest to researchers due to the good thermal stability and easy modulation of sensing performance.

$BiFeO_3$ (BFO) is a typical ABO_3 perovskite material with a rhombohedral structure (*R*3c space group). Studies have been carried out for its applications in magnetoelectric memory, photovoltaic devices, spintronics devices and photocatalysis [11–14]. Researchers also reported the gas sensing performance of BFO to acetone, formaldehyde, oxygen, nitrogen dioxide, isopropanol and so on [15–19]. Xu et al. [20] have studied the gas sensing of BFO nanocrystals to isopropanol. At 240 °C, the response to 100 ppm isopropanol is 31 and the response and recovery time are 6 s and 17 s. Yu et al. [21] have prepared a hierarchical

BFO microcubes-based sensor. The response to 200 ppm acetone is about 5.2 at 240 °C, and the response and recovery times are 10 s and 9 s. Chakraborty et al. [22] have prepared BFO nanoparticles and studied the acetone sensing properties. The response of the prepared sensor to 1 ppm acetone is about 1.8 with great long-term stability of 365 days. According to previous studies, the mechanism for enhanced gas-sensing performance is still controversial. Neogi et al. [23] have prepared an acetone sensor based on yttrium-doped BFO powder, and the prepared sensor shows significant enhancement in response to 200 ppm acetone (~52) and great selectivity and stability for at least 300 days. The primary reason for the enhancement of sensing behavior is the structure and morphology changes induced by moderate yttrium doping. Bala et al. [19] have fabricated Ca^{2+}-doped BFO thin films, and more oxygen vacancy is obtained through doping which enhanced the H_2 sensing characteristics. Sobhan et al. [24] have studied the O_2 sensing performance of Ni^{2+}-doped and Pb^{2+}-doped BFO nanofibers, and claimed that the minor carrier compensation is the key factor affecting gas-sensing performance. Peng et al. [25] have reported a BFO acetone sensor with the ppb detection limit and concluded that the improvement in gas sensitivity is attributed to the morphotropic phase boundary induced by La^{3+} doping. Meanwhile, factors which can improve the gas sensitivity of the BFO sensor are numerous. Tong et al. [17] have reported the gas-sensing performance of BFO nanoparticles had strong dependency on the particle size and morphology. Douani et al. [26] reported that adding carbon fibers can elevate the humidity-sensing property of BFO nanoparticles. Therefore, research should be undertaken on the performance-optimization and enhancement mechanism of BFO gas sensors.

According to earlier reports, the acetone-sensing performance of BFO is related to the structural phase transformation, morphology, and band gap energy which can be modulated by rare-earth ions doping. Herein, $Bi_{1-x}Er_xFeO_3$ particles were synthesized via the sol-gel process and then $Bi_{1-x}Er_xFeO_3$ sensors were fabricated and studied.

2. Experiments

2.1. Synthesis of $Bi_{1-x}Er_xFeO_3$ Nanoparticles

The sol-gel method was used for nanoparticles synthesis. First, $Bi(NO_3)_3{\cdot}5H_2O$ and $Er(NO_3)_3{\cdot}6H_2O$ were dissolved in 10 mL acetic acid at the desired stoichiometry, and stirred for half an hour in a water bath heated to 45 °C. $Fe(NO_3)_3{\cdot}9H_2O$ was dissolved in 10 mL 2-methoxytehanol with the same approach. Then, the two solutions were blended and stirred uniformly via the above method to acquire 0.3 M sol. Finally, the prepared sol was annealed at 625 °C for 30 min to obtain $Bi_{1-x}Er_xFeO_3$ nanoparticles.

2.2. Materials Characterization

The structure of $Bi_{1-x}Er_xFeO_3$ was analyzed by X-ray diffraction (XRD, Smart Lab, Rigaku, Tokyo, Japan). The morphology of $Bi_{1-x}Er_xFeO_3$ nanoparticles were observed by a field-emission scanning electron microscope (SEM, Zeiss Gemini 300, Oberkochen, Germany). The UV-Vis absorption spectrum was measured using a UV-vis spectrophotometer (UV-3600 plus, Shimadzu, Kyoto, Japan). The composition and element valence were characterized by X-ray photoelectron spectroscopy (XPS, Thermo Scientific K-Alpha, Waltham, MA, USA).

2.3. Measurement of $Bi_{1-x}Er_xFeO_3$ Gas Sensors

$Bi_{1-x}Er_xFeO_3$ gas sensors were fabricated by mixing $Bi_{1-x}Er_xFeO_3$ nanoparticles with moderate ethanol to form a smooth slurry, and then spreading the slurry on a ceramic plate on which Ag-Pd interdigital electrodes had been made. Then, the sensors were placed into a muffle furnace (300 °C) for 2 h. Gas-sensing performance was characterized via a multifunctional gas-sensing test system (CGS-MT, Beijing Elite Tech Co., Ltd., Beijing, China). The definition of the sensing response can be expressed by $S = R_g/R_a$, and R_g is the resistance of the sensor in gas. Accordingly, R_a is the resistance in air.

3. Results

3.1. Structure

XRD patterns of $Bi_{1-x}Er_xFeO_3$ nanoparticles were shown in the Figure 1a. When x = 0, $BiFeO_3$ nanoparticles have a rhombohedral perovskite structure (JCPDS No. 86-1518). The (104) and (110) diffraction peaks are broadened as the Er-doping content increases in Figure 1b. According to Debye-Scherrer's formula, the grain size decreases as the full width at half maximum increases. Therefore, it can be speculated that Er doping has led to the reduction of the grain size of nanoparticles, which is also confirmed in the SEM figures. Since the smaller Er^{3+} ions (1.004 Å, CN8) have substituted the larger Bi^{3+} ions (1.17 Å, CN8) which decreases cell parameters and volume, the diffraction peaks of (104) and (110) shift to a higher angle. Meanwhile, they tend to merge to one peak for x = 0.1. In addition, an extra diffraction peak around 25.6° appears in the x = 0.2 sample according to Figure 1a, which indicates phase transformation has occurred. Figure 1c is the enlarged diffraction peak around 39°. The BFO nanoparticles show two diffraction peaks at 38.9° and 39.5°, corresponding to (006) and (202) diffraction peaks of rhombohedral phase, respectively. With the increase of Er-doping content, (006) and (202) gradually merged into one peak for x = 0.2. New diffraction peaks appear around 40° and 42° for x = 0.2. Figure 1d shows the enlarged diffraction peak in the range of 55–61°. The (018) diffraction peak gradually disappeared, and the (214) and (300) merge, and a new diffraction peak was observed at 59° for x = 0.2. These changes of diffraction peaks indicate that the crystal structure had transformed from *R3c* to *Pnma*, which is similar to earlier results [27,28]. Therefore, the diffraction peaks for x = 0.2 sample in Figure 1a are indexed to the orthorhombic phase, which is an isomorph of $LaFeO_3$ (JCPDS No. 04-007-9521). In addition, minor amounts of $Bi_2Fe_4O_9$ and Bi_2O_3 were observed in $Bi_{1-x}Er_xFeO_3$ nanoparticles, and could be ascribed to the heterogeneity of sol during sintering [29,30].

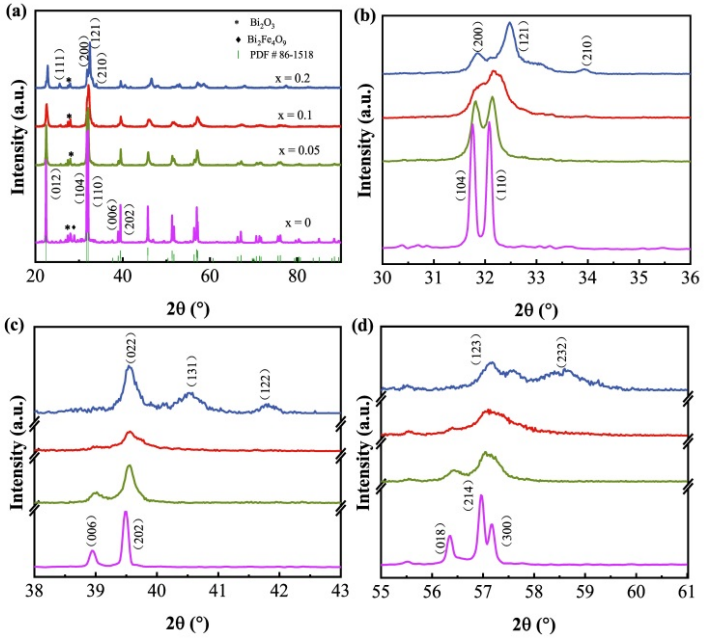

Figure 1. (**a**) XRD patterns of $Bi_{1-x}Er_xFeO_3$ nanoparticles, and the enlarged diffraction peaks (**b**) around 32°, (**c**) ranging from 38° to 43°, (**d**) ranging from 55° to 61°.

3.2. Morphology

Figure 2 shows the SEM images of $Bi_{1-x}Er_xFeO_3$ nanoparticles. The $BiFeO_3$ nanoparticles show irregular shape and uneven grain size. With the increase of Er doping, nanoparticles change to spheres and the size of the nanoparticles decreases by degrees. The average grain size of nanoparticles was 128 nm, 58 nm, 37 nm, and 29 nm, respectively. The decrease of grain size is because smaller Er^{3+} ions have replaced larger Bi^{3+} ions thus increasing the

nucleation rate. The decrease of particle size is conducive to a larger specific area, which can improve the gas sensitivity.

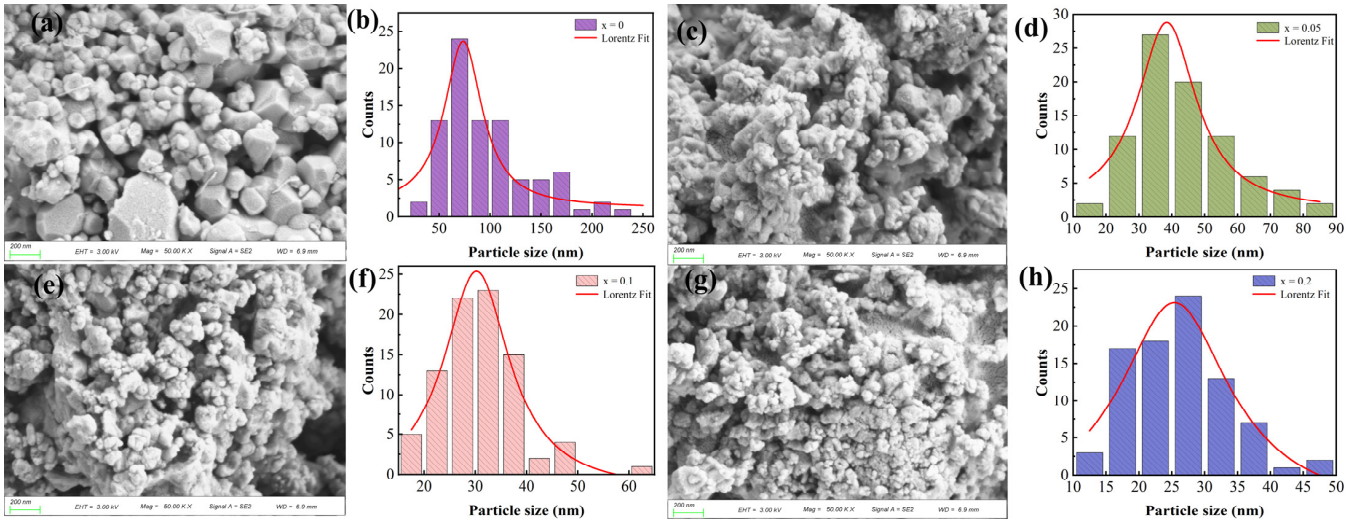

Figure 2. SEM images of $Bi_{1-x}Er_xFeO_3$: (**a**) x = 0, (**c**) x = 0.05, (**e**) x = 0.1 and (**g**) x = 0.2. The size distribution of $Bi_{1-x}Er_xFeO_3$: (**b**) x = 0, (**d**) x = 0.05, (**f**) x = 0.1 and (**h**) x = 0.2.

3.3. Band Gap Energy

UV-vis absorption spectroscopy was performed to obtain the band gap energy E_g of $Bi_{1-x}Er_xFeO_3$ nanoparticles as illustrated in Figure 3a. The relationship between band gap energy E_g and absorption threshold λ_g of a semiconductor is E_g (eV) = 1240/λ_g (nm). The calculated band gap energy is shown in Figure 3b. The E_g decreases with the increase of Er content, and E_g is 2.03, 1.95, 1.89 and 1.83 eV, respectively. Earlier reports have found that smaller E_g can generate larger gas-sensing response [31,32].

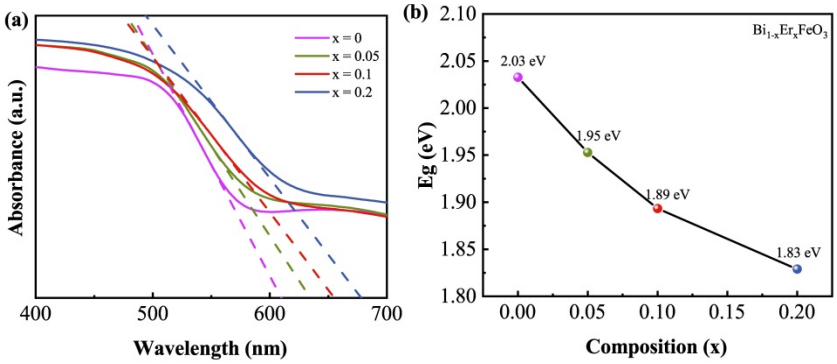

Figure 3. (**a**) Absorption spectra of $Bi_{1-x}Er_xFeO_3$ nanoparticles. (**b**) Band gap energy (E_g) as a function of Er-doping content.

3.4. XPS

Figure 4a is the XPS spectra of $Bi_{1-x}Er_xFeO_3$ nanoparticles. The Bi, Fe, O and C were observed. The inset of Figure 4a shows the peak around 168 eV which is attributed to the Er 4d level of Er^{3+} ions. In Figure 4b, peaks at 711.1 eV and 724.6 eV correspond to the Fe $2p_{3/2}$ level and Fe $2p_{1/2}$ level of the Fe^{3+} state. The two peaks at 158.7 eV and 164.2 eV in Figure 4c are attributed to the Bi $4f_{7/2}$ and Bi $4f_{5/2}$ levels of Bi^{3+} ions. Figure 4d is the XPS spectrum of O 1s. The O 1s spectra of the x = 0 and x = 0.1 samples have been fitted as shown in Figures 4e and 4f. The 530.1 eV peak and 532.1 eV are assigned to the lattice oxygen (denoted by O_L) and absorbed oxygen (denoted by O_a), respectively. The percentage of O_a in x = 0.1 is higher than in x = 0 which suggests Er doping can increase the absorption of oxygen and is beneficial for gas-sensing behavior.

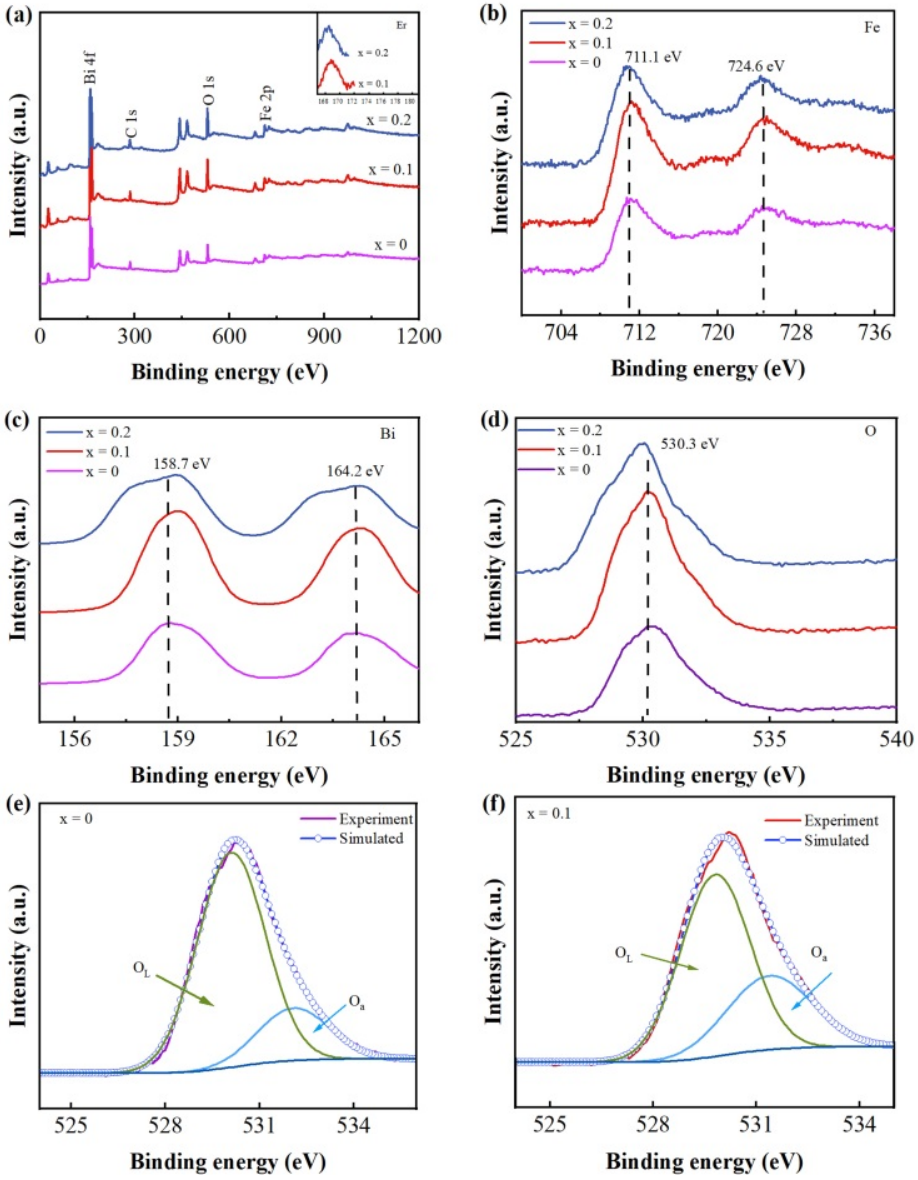

Figure 4. XPS spectra of (**a**) $Bi_{1-x}Er_xFeO_3$ nanoparticles, (**b**) Fe 2p, (**c**) Bi 4f and (**d**) O 1s. The fitted curves of O 1s for (**e**) x = 0, (**f**) x = 0.1.

3.5. Gas-Sensing Performance

Figure 5a is the relation between response to acetone and temperatures. It can be found that $Bi_{0.9}Er_{0.1}FeO_3$ shows the largest response at 300 °C and the responses first rise and then fall. This is because the response of the sensor to acetone gas depends on the relative balance between the adsorption and desorption of the acetone gas and the reaction with the adsorbed oxygen [33,34]. Reaction between acetone molecules and adsorbed oxygen lacks sufficient energy under low temperature, which leads to a poor response. However, the energy of acetone molecules increases because of the increase in temperature, which provides enough energy needed for the reaction, so the response is enhanced. When the temperature increases further, desorption of acetone molecules increases and the acetone absorbed on the nanoparticles is reduced, thus the response is decreased. The optimal operating temperature of Er-doped sensors is lower than that of undoped one (360 °C), as shown in Figure 5b, which demonstrates that Er doping can decrease the optimal operating temperature effectively. The following test was carried out at 300 °C.

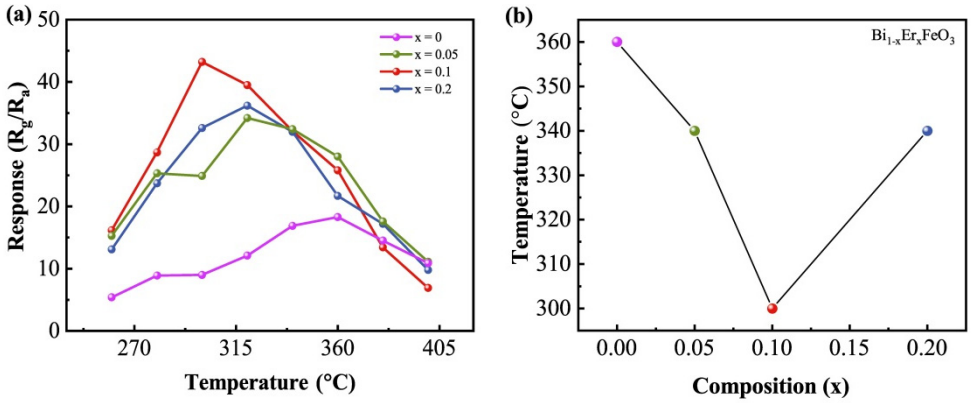

Figure 5. (**a**) Temperature dependence of response of $Bi_{1-x}Er_xFeO_3$ to 100 ppm acetone. (**b**) The optimal operating temperature as a function of Er content.

Figure 6a shows the response of sensors to acetone for different concentration (1, 5, 10, 20, 50, 80, 100, 150 and 200 ppm). The prepared sensors show a low detection limit of 1 ppm to acetone. The relation curve between response and Er-doping content is shown in Figure 6b. With an increase of Er content, the response first increases then decreases, reaching a maximum for x = 0.1 sample. The responses of the $Bi_{0.9}Er_{0.1}FeO_3$ sensor to 1 and 100 ppm acetone are 7 and 43.2 while those of the undoped BFO sensor are 3.2 and 9. The enhanced response is related to the phase transformation of the BFO induced by Er doping. Xing et al. [27] have reported that Er doping would lead to the phase transformation of $Bi_{1-x}Er_xFeO_3$ from *R*3*c* to *Pnma* phase, and the proportion of *Pnma* phase increased with the increase of Er content. When x = 0.05, the proportions of *R*3*c* and *Pnma* phase are 77.6% and 22.3%, respectively. When x = 0.1, the proportions are 58.1% and 41.9%, respectively, and the ratio of the two phase is about 1:1. That means the x = 0.1 sample is at the so-called morphotropic phase boundary (MPB) and has the largest lattice distortion. When x = 0.2, only *Pnma* phase exists. According to a previous study, large lattice distortion will decrease the electron effective mass and scattering probability. The carrier concentration and electron mobility are inversely proportional to the two parameters. The increase of carrier concentration and electron mobility will lead to a thicker hole-accumulation layer at the surface of the nanoparticles, and bring more changes for the accumulation layer. Therefore, the changes in resistance of the senor increase and the acetone-sensing performance is improved. This phenomenon has also been reported in the La^{3+}-doped BFO gas sensor [25].

Meanwhile, the morphology of nanoparticles is considered to have an effect on the response of the $Bi_{1-x}Er_xFeO_3$ sensor. The specific area of nanoparticles increases and more active sites generate, thus more gas molecules will be absorbed. That explains why all doped samples show larger responses than the pure BFO. However, the x = 0.2 sample shows the smallest grain size while the response is not the largest. As a result, we conclude that morphology is not the dominating factor to improve acetone-sensing performance for $Bi_{1-x}Er_xFeO_3$ sensors. In addition, Er doping has decreased the band gap energy of nanoparticles which may have contributed to the enhancement of the acetone-sensing response.

The transient response of the $Bi_{0.9}Er_{0.1}FeO_3$ sensor to 100 ppm acetone is shown in Figure 6c. Response time (τ_{res}) refers to the amount of time that the resistance of the $Bi_{1-x}Er_xFeO_3$ sensor goes from R_a to $R_a + | R_a\text{-}R_g | \times 90\%$. Recovery time ($\tau_{recov}$) is defined as the time needed from R_g to $R_g - | R_a\text{-}R_g | \times 90\%$. The τ_{res} and τ_{recov} of the $Bi_{0.9}Er_{0.1}FeO_3$ sensor are about 4 s and 14 s, which is close to an earlier report [17]. Figure 6d is the response of the $Bi_{0.9}Er_{0.1}FeO_3$ sensor to 100 ppm acetone measured for six cycles, demonstrating good stability. The stability of the $Bi_{0.9}Er_{0.1}FeO_3$ sensor to 50 ppm of acetone was measured randomly within a month (on day 1, 6, 15, 16, 27 and 29) as shown in Figure 6e. The measurement was carried out at 300 °C. The response has changed

little in a month, suggesting the great long-term stability of the prepared gas sensor. Figure 6f is the current-voltage (*I-V*) characteristics of the $Bi_{0.9}Er_{0.1}FeO_3$ sensor tested at 270–360 °C. The current is linearly varying with voltage. Thus the conduction mechanism of the sensor is an ohmic conduction mechanism and the key factor in gas sensing is $Bi_{0.9}Er_{0.1}FeO_3$ nanoparticles. Meanwhile, the *I-V* curves show no deformation as the operating temperature increases which means the prepared sensor can be applied at high temperatures.

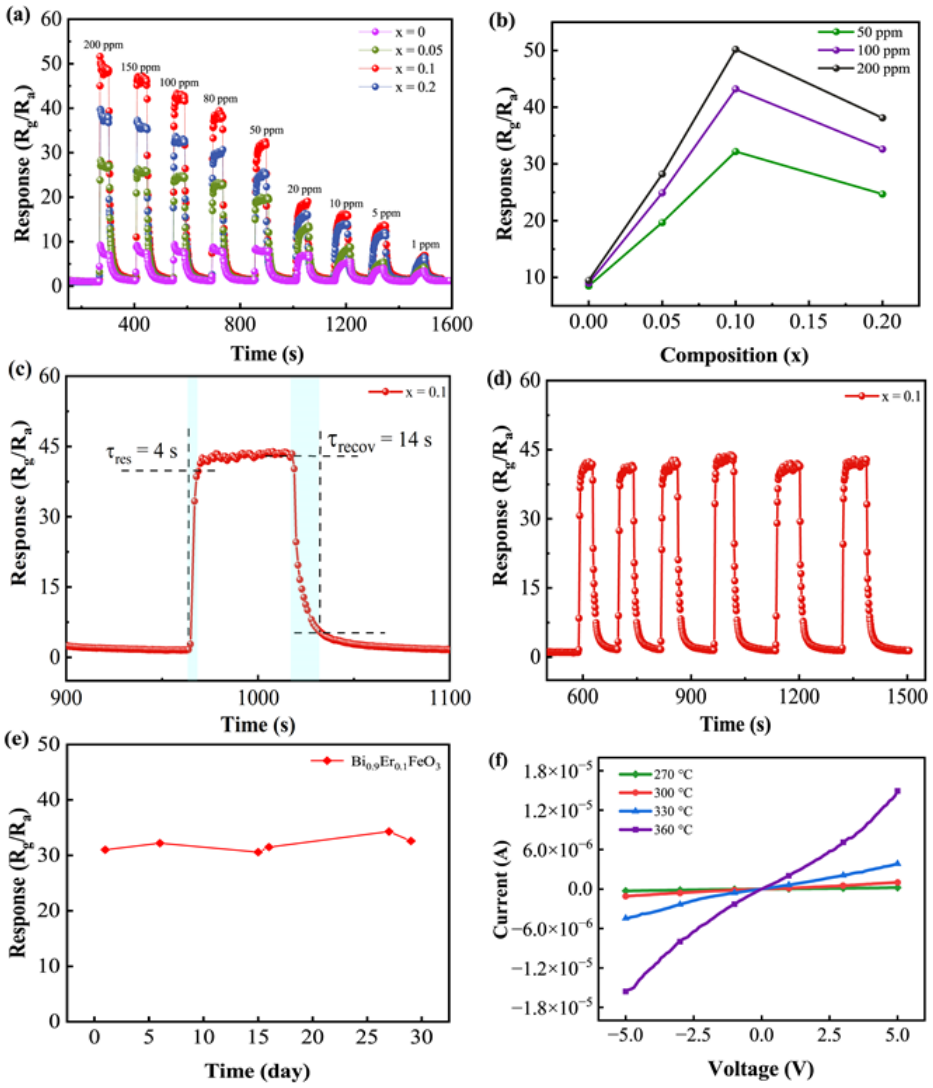

Figure 6. (**a**) Dynamic response and recovery curves of $Bi_{1-x}Er_xFeO_3$ sensors to acetone. (**b**) Response of sensors as a function of Er-doping content. (**c**) Transient response of $Bi_{0.9}Er_{0.1}FeO_3$ sensor to 100 ppm acetone. (**d**) The response to 100 ppm acetone measured for six cycles. (**e**) Stability measurement of $Bi_{0.9}Er_{0.1}FeO_3$ sensor to 50 ppm acetone within a month. (**f**) Current-voltage characteristics of $Bi_{0.9}Er_{0.1}FeO_3$ sensor at different temperatures.

The selectivity of gas sensors has been characterized by measuring responses in acetone, methanol, ethanol, benzene, methylbenzene, xylene, ammonia and triethylamine (concentration = 100 ppm) as seen in Figure 7. The undoped BFO sensor demonstrated the minimum differences of responses to all gases thus the worst selectivity. The x = 0.1 sample shows the largest response to all gases, and the response to acetone was significantly higher than the others. For all sensors, the response to acetone is the largest followed by alcohols, triethylamine and ammonia, and the response to benzene and its derivatives are minimum.

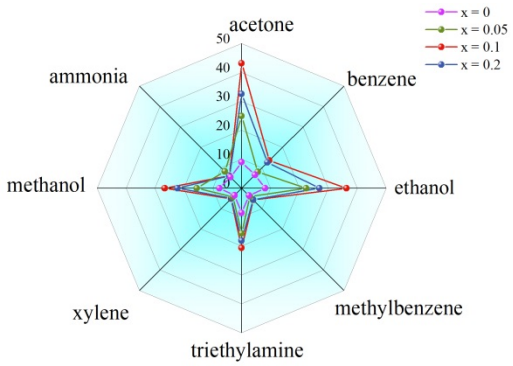

Figure 7. Selectivity of $Bi_{1-x}Er_xFeO_3$ sensors to different gases.

4. Discussion

Figure 8 illustrates the possible mechanism and the principle is explained by Equations (1)–(5), where O^-, e^- and h^+ represent oxygen ions, electrons and holes, respectively. BFO and Er-doped BFO are generally considered to be p-type semiconductors. As shown in Figure 8a, in air, O_2 is absorbed on the BFO nanoparticles and captures electrons from particles, forming O^-. Thus, a hole-accumulation layer is obtained at the surface (Equations (1) and (2)). Consequently, the energy band is lowered at the surface, resulting in a decrease in resistance. When BFO sensors are exposed in reducing air acetone, the acetone molecule will react with O^- to release electrons to nanoparticles. Those released electrons recombine with holes and the resistance increases (Equations (3)–(5)).

$$O_{2(gas)} = O_{2(ads)}, \quad (1)$$

$$O_{2(ads)} + 2e^- = 2O^-_{(ads)}, \quad (2)$$

$$CH_3COCH_{3(gas)} \rightarrow CH_3COCH_{3(ads)}, \quad (3)$$

$$CH_3COCH_{3(ads)} + 8O^-_{(ads)} \rightarrow 3CO_2 + 3H_2O + 8e^-, \quad (4)$$

$$h^+ + e^- = \text{null}. \quad (5)$$

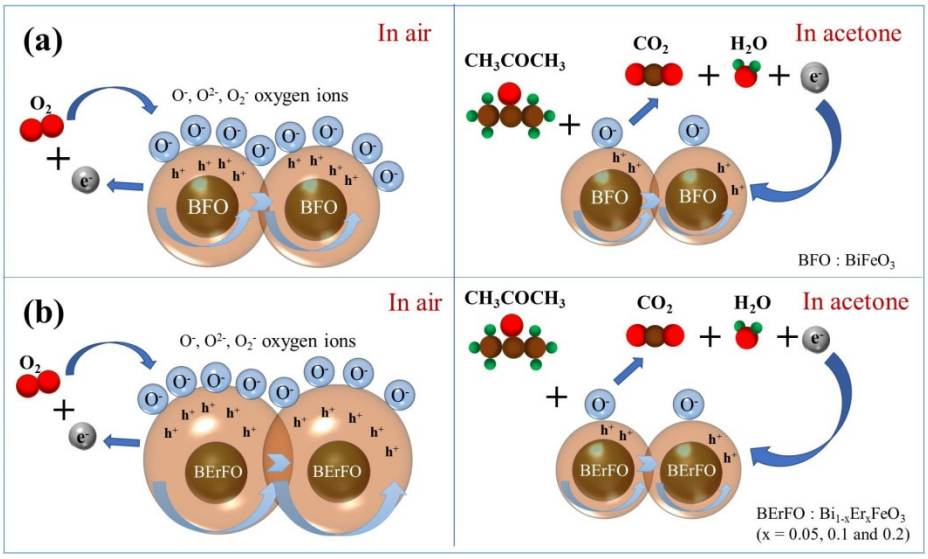

Figure 8. The illustration of the gas-sensing mechanism of $Bi_{1-x}Er_xFeO_3$ sensors: (**a**) x = 0, (**b**) x = 0.05, 0.1, 0.2.

When BFO nanoparticles are doped with Er^{3+} ions, phase transformation and lattice distortion occur which increase the carrier concentration and mobility. Consequently,

recombination of electrons and holes is reduced and the hole-accumulation layer is widened. As a result, more oxygen will be absorbed. When the $Bi_{1-x}Er_xFeO_3$ sensor is exposed to acetone, larger changes of resistance and responses are obtained, as shown in Figure 8b.

5. Conclusions

$Bi_{1-x}Er_xFeO_3$ nanoparticles were synthesized via the facile sol-gel process. Er doping has resulted in the transformation from rhombohedral phase to orthorhombic phase. Meanwhile, the nanoparticle size and band gap energy decreased with the increase of Er-doping content, which is beneficial for the improvement of acetone-sensing performance. The $Bi_{0.9}Er_{0.1}FeO_3$ is located at the MPB and displays the optimum response to 100 ppm acetone (43.2) at 300 °C, which is 4.8 times that of pure BFO. In addition, the $Bi_{0.9}Er_{0.1}FeO_3$ sensor shows fast response and recovery, the τ_{res} and τ_{recov} of the $Bi_{0.9}Er_{0.1}FeO_3$ sensor are about 4 s and 14 s. The phase transformation is considered to have played the key role in the enhanced acetone-sensing performance for the $Bi_{1-x}Er_xFeO_3$ sensors.

Author Contributions: Conceptualization, X.L. and G.W.; methodology, J.L.; writing—original draft preparation, J.L.; writing—review and editing, X.L. and L.G.; supervision, G.W.; funding acquisition, X.L. and G.W. All authors have read and agreed to the published version of the manuscript.

Funding: This work was supported by the National Natural Science Foundation of China (Grant No. 62173128), the Key Project of Scientific and Technology Research of Henan Province (Grant No. 212102210224), the Innovation Team of Henan Province (Grant No. 21IRTSTHN016), and the Program of Henan Polytechnic University (Grant No. B2014-020, 2019XQG-06).

Data Availability Statement: Not applicable.

Conflicts of Interest: The authors declare no conflict of interest.

References

1. Amiri, V.; Roshan, H.; Mirzaei, A.; Neri, G.; Ayesh, A.I. Nanostructured metal oxide-based acetone gas sensors: A Review. *Sensors* **2020**, *20*, 3096. [CrossRef] [PubMed]
2. Rydosz, A. Sensors for enhanced detection of acetone as a potential tool for noninvasive diabetes monitoring. *Sensors* **2018**, *18*, 2298. [CrossRef] [PubMed]
3. Hsu, K.-C.; Fang, T.-H.; Hsiao, Y.-J.; Li, Z.-J. Rapid detection of low concentrations of H_2S using CuO-doped ZnO nanofibers. *J. Alloy Compd.* **2021**, *852*, 157014. [CrossRef]
4. Van Toan, N.; Hung, C.M.; Hoa, N.D.; Van Duy, N.; Thi Thanh Le, D.; Thi Thu Hoa, N.; Viet, N.N.; Phuoc, P.H.; Van Hieu, N. Enhanced NH_3 and H_2 gas sensing with H_2S gas interference using multilayer SnO_2/Pt/WO_3 nanofilms. *J. Hazard. Mater.* **2021**, *412*, 125181. [CrossRef]
5. Zhou, Q.; Lin, Y.; Zhang, K.; Li, M.; Tang, D. Reduced graphene oxide/$BiFeO_3$ nanohybrids-based signal-on photoelectrochemical sensing system for prostate-specific antigen detection coupling with magnetic microfluidic device. *Biosens. Bioelectron.* **2018**, *101*, 146–152. [CrossRef]
6. Guo, L.; Wang, Y.; Shang, Y.; Yang, X.; Zhang, S.; Wang, G.; Wang, Y.; Zhang, B.; Zhang, Z. Preparation of Pd/PdO@ZnO-ZnO nanorods by using metal organic framework templated catalysts for selective detection of triethylamine. *Sens. Actuators B Chem.* **2022**, *350*, 130840. [CrossRef]
7. Guo, L.; Wang, Y.; Zeng, H.; Feng, Y.; Yang, X.; Zhang, S.; Xu, Y.; Wang, G.; Wang, Y.; Zhang, Z. Rational design of SnO_2 hollow microspheres functionalized with derivatives of Pt loaded MOFs for superior formaldehyde detection. *Nanomaterials* **2022**, *12*, 1881. [CrossRef]
8. Qin, W.; Yuan, Z.; Gao, H.; Zhang, R.; Meng, F. Perovskite-structured $LaCoO_3$ modified ZnO gas sensor and investigation on its gas sensing mechanism by first principle. *Sens. Actuators B Chem.* **2021**, *341*, 130015. [CrossRef]
9. Cao, S.; Zeng, W.; Zhang, H.; Li, Y. Hydrothermal synthesis of SnO_2 nanocubes and nanospheres and their gas sensing properties. *J. Mater. Sci. Mater. Electron.* **2015**, *26*, 2871–2878. [CrossRef]
10. Wang, H.; Li, H.; Li, S.; Liu, L.; Wang, L.; Guo, X. Fabrication of hollow In_2O_3–ZnO microtubules by a simple biotemplate method and their gas-sensing properties. *J. Mater. Sci. Mater. Electron.* **2016**, *28*, 958–962. [CrossRef]
11. Pang, K.; Zhang, Q.; Xu, Y. Hierarchical magnetic $BiFeO_3$ microcages: Controlling synthesis and visible-light photocatalytic activity. *Ceram. Int.* **2019**, *45*, 1554–1561. [CrossRef]
12. Khan, A.H.; Atiq, S.; Mahmood, A.; Ramay, S.M.; Kumail Abbas, S.; Naseem, S. Optimisation of giant magnetoresistance in Mn-substituted $BiFeO_3$ for low field sensors. *Ceram. Int.* **2018**, *44*, 14677–14685. [CrossRef]
13. Liu, X.; Wang, G.; Wu, J.; Li, M.; Pu, S.; Hu, Z. Enhanced multiferroic properties of $Bi_{0.85}Nd_{0.15}FeO_3$ ceramics with excess Bi_2O_3. *J. Alloy. Compd.* **2019**, *791*, 200–207. [CrossRef]

14. Yin, L.; Mi, W. Progress in $BiFeO_3$-based heterostructures: Materials, properties and applications. *Nanoscale* **2020**, *12*, 477–523. [CrossRef]
15. Zhang, Y.; Xu, H.; Dong, S.; Han, R.; Liu, X.; Wang, Y.; Li, S.; Bu, Q.; Li, X.; Xiang, J. A fast response & recovery acetone gas sensor based on $BiFeO_3$ nanomaterials with high sensitivity and low detection limit. *J. Mater. Sci. Mater. Electron.* **2017**, *29*, 2193–2200. [CrossRef]
16. Abisegapriyan, K.S.; Raj, N.P.M.J.; Alluri, N.R.; Chandrasekhar, A.; Kim, S.-J. All in one transitional flow-based integrated self-powered catechol sensor using $BiFeO_3$ nanoparticles. *Sens. Actuators B Chem.* **2020**, *320*, 128417. [CrossRef]
17. Tong, T.; Chen, J.; Jin, D.; Cheng, J. Preparation and gas sensing characteristics of $BiFeO_3$ crystallites. *Mater. Lett.* **2017**, *197*, 160–162. [CrossRef]
18. Poghossian, A.S.; Abovian, H.V.; Avakian, P.B.; Mkrtchian, S.H.; Haroutunian, V.M. Bismuth ferrites: New materials for semiconductor gas sensors. *Sens. Actuators B Chem.* **1991**, *4*, 545–549. [CrossRef]
19. Bala, A.; Majumder, S.B.; Dewan, M.; Roy Chaudhuri, A. Hydrogen sensing characteristics of perovskite based calcium doped $BiFeO_3$ thin films. *Int. J. Hydrogen Energy* **2019**, *44*, 18648–18656. [CrossRef]
20. Xu, H.; Xu, J.; Wei, J.; Zhang, Y. Fast response isopropanol sensing properties with sintered $BiFeO_3$ nanocrystals. *Materials* **2020**, *13*, 3829. [CrossRef]
21. Yu, Q.; Zhang, Y.; Xu, Y. Hierarchical hollow $BiFeO_3$ microcubes with enhanced acetone gas sensing performance. *Dalton Trans.* **2021**, *50*, 6702–6709. [CrossRef]
22. Chakraborty, S.; Pal, M. Highly selective and stable acetone sensor based on chemically prepared bismuth ferrite nanoparticles. *J. Alloy. Compd.* **2019**, *787*, 1204–1211. [CrossRef]
23. Neogi, S.; Ghosh, R. Origin of irreversible to reversible transition in acetone detection for Y-doped $BiFeO_3$ perovskite. *J. Appl. Phys.* **2020**, *128*, 144501. [CrossRef]
24. Sobhan, M.; Xu, Q.; Katoch, A.; Anariba, F.; Kim, S.S.; Wu, P. O_2 sensing dynamics of $BiFeO_3$ nanofibers: Effect of minor carrier compensation. *Nanotechnology* **2015**, *26*, 175501. [CrossRef]
25. Peng, S.; Ma, M.; Yang, W.; Wang, Z.; Wang, Z.; Bi, J.; Wu, J. Acetone sensing with parts-per-billion limit of detection using a $BiFeO_3$-based solid solution sensor at the morphotropic phase boundary. *Sens. Actuators B Chem.* **2020**, *313*, 128060. [CrossRef]
26. Douani, R.; Lamrani, N.; Oughanem, M.H.; Saidi, M.; Guhel, Y.; Chaouchi, A.; Boudart, B. Improvement of humidity sensing performance of $BiFeO_3$ nanoparticles-based sensor by the addition of carbon fibers. *Sens. Actuators A Phys.* **2020**, *307*, 111981. [CrossRef]
27. Xing, W.; Ma, Y.; Bai, Y.; Zhao, S. Enhanced ferromagnetism of Er-doped $BiFeO_3$ thin films derived from rhombohedral-to-orthorhombic phase transformations. *Mater. Lett.* **2015**, *161*, 216–219. [CrossRef]
28. Rani, S.; Sanghi, S.; Agarwal, A.; Kumar, R.; Singh, O. Crystal structure, magnetic and dielectric properties of Er-doped $BiFeO_3$ ceramics. *Appl. Phys. A* **2022**, *128*, 576. [CrossRef]
29. Iorgu, A.I.; Maxim, F.; Matei, C.; Ferreira, L.P.; Ferreira, P.; Cruz, M.M.; Berger, D. Fast synthesis of rare-earth (Pr^{3+}, Sm^{3+}, Eu^{3+} and Gd^{3+}) doped bismuth ferrite powders with enhanced magnetic properties. *J. Alloy Compd.* **2015**, *629*, 62–68. [CrossRef]
30. Wrzesinska, A.; Khort, A.; Bobowska, I.; Busiakiewicz, A.; Wypych-Puszkarz, A. Influence of the La^{3+}, Eu^{3+}, and Er^{3+} doping on structural, optical, and electrical properties of $BiFeO_3$ nanoparticles synthesized by microwave-assisted solution combustion method. *J. Nanomater.* **2019**, *2019*, 5394325. [CrossRef]
31. Cui, S.; Pu, H.; Wells, S.A.; Wen, Z.; Mao, S.; Chang, J.; Hersam, M.C.; Chen, J. Ultrahigh sensitivity and layer-dependent sensing performance of phosphorene-based gas sensors. *Nat. Commun.* **2015**, *6*, 8632. [CrossRef] [PubMed]
32. Pei, S.; Ma, S.; Xu, X.; Xu, X.; Almamoun, O. Modulated $PrFeO_3$ by doping Sm^{3+} for enhanced acetone sensing properties. *J. Alloy. Compd.* **2021**, *856*, 158274. [CrossRef]
33. Hjiri, M.; El Mir, L.; Leonardi, S.G.; Pistone, A.; Mavilia, L.; Neri, G. Al-doped ZnO for highly sensitive CO gas sensors. *Sens. Actuators B Chem.* **2014**, *196*, 413–420. [CrossRef]
34. Li, X.; Li, D.; Xu, J.; Jin, H.; Jin, D.; Peng, X.; Hong, B.; Li, J.; Yang, Y.; Ge, H.; et al. Calcination-temperature-dependent gas-sensing properties of mesoporous nickel oxides nanowires as ethanol sensors. *Powder Technol.* **2017**, *318*, 40–45. [CrossRef]